Proposal on Model Based Current Overshoot Suppression of Receiver Side Coil in Drone Wireless Power Transfer System

Kota Fujimoto
Graduate School of Frontier Sciences
The University of Tokyo
Kashiwa, Japan
fujimoto.kota21@ae.k.u-tokyo.ac.jp

Takumi Hamada
Graduate School of Frontier Sciences
The University of Tokyo
Kashiwa, Japan
hamada.takumi21@ae.k.u-tokyo.ac.jp

Hiroshi Fujimoto
Graduate School of Frontier Sciences
The University of Tokyo
Kashiwa, Japan
fujimoto@k.u-tokyo.ac.jp

***Abstract*—This paper proposes a model-based control method in the wireless power transfer (WPT) system by operating a semi-bridgeless active rectifier (SBAR) to suppress the secondary coil current overshoot. By damping the current overshoot, it is possible to reduce the rectifier's rated current and decrease the rectifier's size, which is beneficial for the lightweight-oriented system such as drones. In the control method, an inverse of the plant model is used to calculate the reference input to the system. The current overshoot is reduced by operating the SBAR under the duty ratio calculated from the model. To confirm the performance of the proposed method, the simulation and the experiment using the WPT prototype are conducted. The experimental results show that the proposed method can suppress the secondary coil current overshoot. The results suggest it is possible to realize the lighter secondary system by applying the proposed method.**

***Index Terms*—wireless power transfer, semi-bridgeless active rectifier, overshoot suppression, current control**

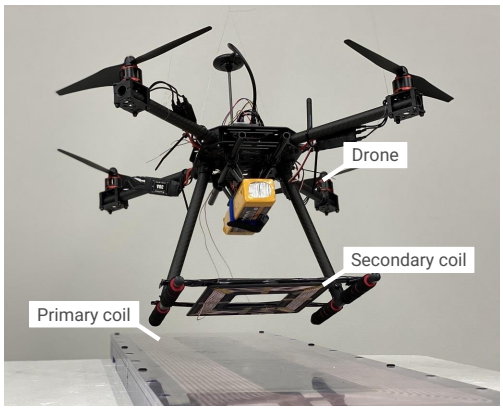

Fig. 1. Diagram of the drone in-flight charging system.

I. Introduction

There are some studies that aim to realize the wireless power transfer (WPT) system for a flying drone. The feasibility of applying the WPT system to a flying drone is verified in [1] to extend the flight duration, in which the microwave beam is implemented as an energy medium. The main bottleneck for the microwave WPT system for drones is low efficiency, and recently there have been several studies that have tried to improve the system efficiency. In [2], the port-to-port efficiency is $31.4\,\%$, which is not practically sufficient for drones. On the other hand, some studies show that a magnetic resonant circuit helps realize the WPT system for flying drones [3]–[6]. In [3], the average link efficiency, which is the same role as a port-to-port efficiency, is approximately $90\,\%$ despite the dynamic conditions of flying drones. Although they both have their advantages, it is generally said that the magnetic resonant WPT system is more efficient than the microwave WPT system. Fig. 1 shows a diagram of the drone wireless in-flight charging system with the magnetic resonant WPT system. To realize this system, it is needed to make the secondary system as light as possible.

A magnetic resonant WPT system has a rectifier on the secondary side. In the drone wireless in-flight charging system, it could happen that excessive current flows into the battery due to a sudden change of the mutual inductance. Therefore, it is necessary to choose a lighter and a power-controllable rectifying system to realize the in-flight charging system. There are several types of rectifiers, such as a full-bridge diode rectifier [7], a full-bridge active rectifier with semiconductor switches [8], [9], and a semi-bridgeless active rectifier (SBAR) [10]–[12], which has two diodes and two semiconductor switches as shown in Fig. 2. Using a full-bridge diode rectifier, it is unavoidable to load a DC-DC converter to control the power to a battery, which increases the weight of drones. Although it is possible to control the load power by using a full-bridge active rectifier without a DC-DC converter, the system becomes more complex and expensive than an SBAR. On the other hand, an SBAR does not need a DC-DC converter, and it is composed of only two semiconductor switches. Therefore, an SBAR is the most suitable for a drone WPT system in terms of weight and simplicity.

The SBAR often operates with an unsynchronized ON-OFF switching method [13]. This method can be easily implemented as it does not need an alternative current sensor. The operation circuit diagram of the SBAR is shown in Fig. 2. The transferred secondary AC current is rectified at the SBAR

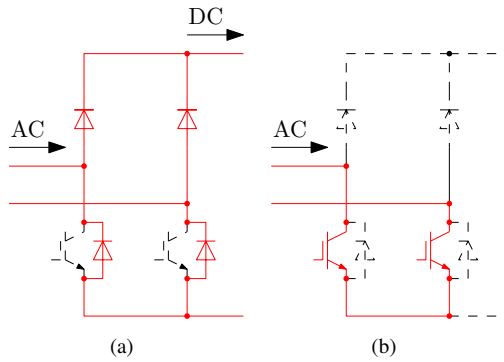

Fig. 2. Circuit diagram of the SBAR. (a) Rectification mode (b) Short mode

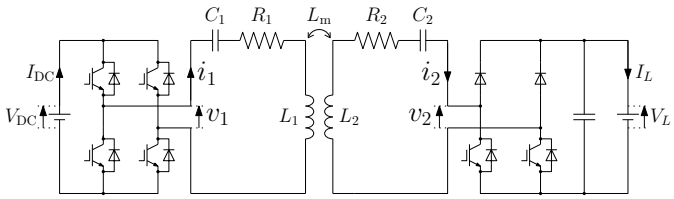

Fig. 3. Circuit diagram of the magnetic resonant WPT system with the SBAR.

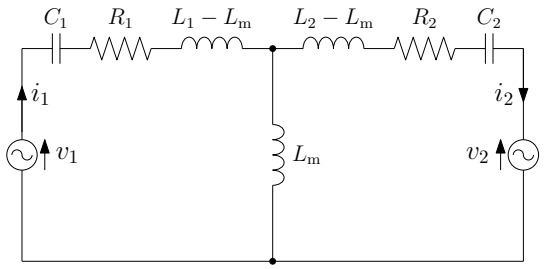

Fig. 4. Equivalent circuit model of the WPT part.

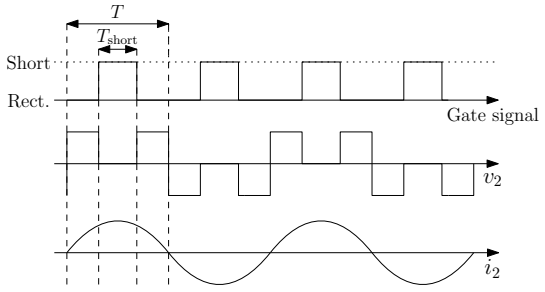

Fig. 5. Ideal operating waveforms of the SBAR.

with rectification mode (RM) to charge the battery as shown in Fig. 2(a). When the battery is fully charged, the SBAR operation mode is switched to short mode (SM) as shown in Fig. 2(b), so that the current flow to the battery is cut off. By changing the operation mode, it is possible to prevent the battery from overcharging. However, when the mode switches from the RM to the SM, the secondary coil current overshoot occurs. There have been no studies addressing this problem. To avoid raising the rated current and increasing the size of the rectifier, we focus on the overshoot suppression in the SBAR system with an unsynchronized ON-OFF switching method.

This paper focuses on the secondary coil current control to resolve the above problem. By switching between the RM and the SM alternately and gradually extending the SM period, it is possible to suppress the coil current overshoot. The model of the WPT system derived in this paper determines the ratio of the SM period to the operation period. The experimental results show that the overshoot is suppressed by applying the control method to the SBAR system.

II. Topology analysis

The circuit used in this paper is shown in Fig. 3. The circuit consists of a direct current (DC) voltage source, full-bridge inverter, series-series compensated resonant circuit, SBAR, and smoothing capacitor. v and i are the instantaneous value of the voltage and current, V and I are the fundamental amplitude of v and i, L, C, and R are self-inductance, resonant capacitor, and internal resistor, respectively. The subscript 1, 2 represent the value of the primary side, the secondary side, respectively. V_{DC}, I_{DC} and V_{L}, I_{L} are the value of the primary DC voltage and current, and the secondary DC voltage and current. Fig. 4 is the equivalent circuit of the system shown in Fig. 3. The circuit equation is expressed as follows:

$$v_1 = R_1 i_1 + \frac{1}{C_1}\int i_1 \mathrm{d}t + L_1 \frac{\mathrm{d}i_1}{\mathrm{d}t} - L_{\mathrm{m}} \frac{\mathrm{d}i_2}{\mathrm{d}t}, \tag{1a}$$

$$v_2 = -R_2 i_2 - \frac{1}{C_2}\int i_2 \mathrm{d}t - L_2 \frac{\mathrm{d}i_2}{\mathrm{d}t} + L_{\mathrm{m}} \frac{\mathrm{d}i_1}{\mathrm{d}t}. \tag{1b}$$

Under the resonant condition, focusing on the fundamental component, the waveforms are expressed as

$$i_1 = I_1(t)\sin\omega t, \tag{2a}$$

$$v_1 = V_1(t)\sin\omega t, \tag{2b}$$

$$i_2 = I_2(t)\cos\omega t, \tag{2c}$$

$$v_2 = V_2(t)\cos\omega t. \tag{2d}$$

ω is the angular frequency of the inverter, which equals to the resonant frequency of the primary and secondary circuit. By substituting (2) into (1), the following equations are obtained:

$$2L_1 \frac{\mathrm{d}I_1(t)}{\mathrm{d}t} + R_1 I_1 + \omega L_{\mathrm{m}} I_2 - V_1 = 0, \tag{3a}$$

$$2L_2 \frac{\mathrm{d}I_2(t)}{\mathrm{d}t} + R_2 I_2 - \omega L_{\mathrm{m}} I_1 - V_2 = 0. \tag{3b}$$

These equations are derived under the approximation that the frequency of the current envelope is sufficiently smaller than the operating frequency.

The Laplace form of the equations (3) are shown as

$$2L_1 s I_1(s) + R_1 I_1(s) + \omega L_{\mathrm{m}} I_2(s) + V_1(s) = 0, \tag{4a}$$

$$2L_2 s I_2(s) + R_2 I_2(s) - \omega L_{\mathrm{m}} I_1(s) + V_2(s) = 0. \tag{4b}$$

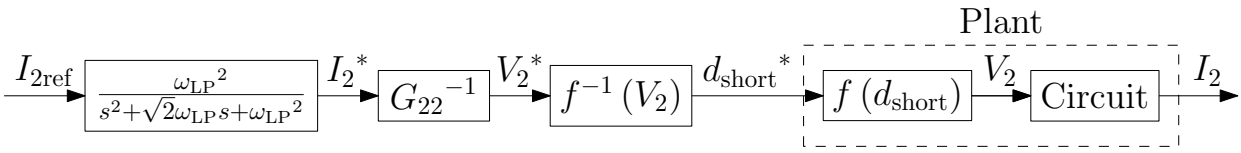

Fig. 6. Block diagram of the control system.

TABLE I
CIRCUIT PARAMETERS

Parameter	Value
Primary inductance L_1	236 µH
Secondary inductance L_2	18.9 µH
Mutual inductance L_{m}	6.25 µH
Primary resistor R_1	108 mΩ
Secondary resistor R_2	32.5 mΩ
Input voltage V_{DC}	30 V
Load voltage V_L	30 V
Resonance frequency f	85 kHz

By solving (4), $I_1(s)$ and $I_2(s)$ are expressed as

$$I_1(s) = \frac{(\alpha_1 s + \beta_1) V_1(s)}{s^2 + 2\zeta\omega_{\mathrm{n}} s + {\omega_{\mathrm{n}}}^2} - \frac{\gamma V_2(s)}{s^2 + 2\zeta\omega_{\mathrm{n}} s + {\omega_{\mathrm{n}}}^2}, \quad (5a)$$

$$I_2(s) = \frac{\gamma V_1(s)}{s^2 + 2\zeta\omega_{\mathrm{n}} s + {\omega_{\mathrm{n}}}^2} - \frac{(\alpha_2 s + \beta_2) V_2(s)}{s^2 + 2\zeta\omega_{\mathrm{n}} s + {\omega_{\mathrm{n}}}^2}, \quad (5b)$$

where ζ, ω_{n}, α_1, β_1, α_2, β_2, and γ are shown as

$$\begin{aligned} \zeta &= \frac{L_1R_2 + L_2R_1}{\sqrt{4L_1L_2}} \cdot \frac{1}{\sqrt{R_1R_2 + (\omega L_{\mathrm{m}})^2}}, \\ \omega_{\mathrm{n}} &= \frac{1}{2}\sqrt{\frac{R_1R_2 + (\omega L_{\mathrm{m}})^2}{L_1L_2}}, \\ \alpha_1 &= \frac{1}{2L_1}, \quad \beta_1 = \frac{R_2}{4L_1L_2}, \\ \alpha_2 &= \frac{1}{2L_2}, \quad \beta_2 = \frac{R_1}{4L_1L_2}, \quad \gamma = \frac{\omega L_{\mathrm{m}}}{4L_1L_2}. \end{aligned} \quad (6)$$

III. CONTROL STRATEGY FOR CURRENT OVERSHOOT SUPPRESSION

This section describes how the SBAR is operated. Fig. 5 shows the ideal operating waveforms of the SBAR. It shows the gate signal sent to the lower arm of the rectifier, the secondary voltage v_2, and the secondary current i_2, respectively. T is the rectifier's operating period. In this paper, T is defined as a half of the switching period of the primary inverter. T_{short} is the short period in T in which the lower arm of the rectifier is on. During this period, the power is not transferred to the load side. The duty ratio of the rectifier d_{short} is defined as

$$d_{\mathrm{short}} = \frac{T_{\mathrm{short}}}{T}. \quad (7)$$

By deciding d_{short}, the operation of the rectifier is determined.

According to (5b), the transfer function from V_2 to I_2 is expressed as follows:

$$G_{22} = \frac{I_2(s)}{V_2(s)} = -\frac{\alpha_2 s + \beta_2}{s^2 + 2\zeta\omega_{\mathrm{n}} s + {\omega_{\mathrm{n}}}^2}. \quad (8)$$

When a step signal of V_2 is input to the system by switching the SBAR from the RM to the SM, the coil current overshoot occurs because ζ is too small in a typical magnetic resonant WPT system. In order to suppress the overshoot in the step response of I_2, this paper proposes a SBAR control method. By controlling V_2 appropriately, the overshoot can be suppressed.

Fig. 6 is the block diagram of the control system, which shows how the SBAR is operated. $I_{2\mathrm{ref}}$, ${I_2}^*$, ${V_2}^*$, and ${d_{\mathrm{short}}}^*$ are the secondary current's reference value, the secondary current's calculated value, the secondary voltage's calculated value, and the calculated value of the duty ratio of the rectifier, respectively. $f(d_{\mathrm{short}})$ is the function showing the relation between V_2 and d_{short}, which is defined as

$$V_2 = f(d_{\mathrm{short}}) = \frac{4}{\pi} V_L \left\{1 - \sin\left(\frac{\pi}{2} d_{\mathrm{short}}\right)\right\}. \quad (9)$$

(9) is derived as the difference between the fundamental wave amplitude of the square wave and the fundamental wave amplitude of the square wave when operating the rectifier with a phase-shift control. $f^{-1}(V_2)$ is the inversion of $f(d_{\mathrm{short}})$. In this paper, ${V_2}^*$ is calculated using the inversion system of G_{22}. ${G_{22}}^{-1}$ is the non-proper system, so the low-pass filter shown in Fig. 6 is placed before ${G_{22}}^{-1}$. Applying this scheme to the operation, the proposed method, in which the secondary coil current overshoot at the transition phase from the RM to the SM is suppressed, is implemented.

IV. SIMULATION AND EXPERIMENT

In order to validate the effectiveness of the proposed method, the simulation is carried out at first. The parameter is listed in TABLE I. Figs. 7(a), 7(b), and 7(c) show the reference values of ${V_2}^*$ considered in the simulation. Each figure shows a step-type reference value, a ramp-type reference value, and a proposed reference value calculated using the model as shown in Fig. 6, respectively. The slope of the ramp-type reference value is decided such that the time constant is the same as that of the proposed method.

Figs. 7(d), 7(e), and 7(f) show the simulation results. All the waveforms once converge at $4\,\mathrm{ms}$. The convergence of the secondary coil current amplitude at $4\,\mathrm{ms}$ is $10.5\,\mathrm{A}$. The waveforms after $4\,\mathrm{ms}$ are shown because the proposed reference value converges around $14\,\mathrm{ms}$.

Fig. 7(d) shows that the maximum current amplitude is tremendously large if there is no controller in the secondary system. Fig. 7(e) shows that the ramp-type reference trajectory cannot wholly suppress the overshoot. On the other hand, Fig. 7(f) shows that the proposed method can completely suppress the overshoot. It is because the inverse of the plant model is implemented in the control system, which is able

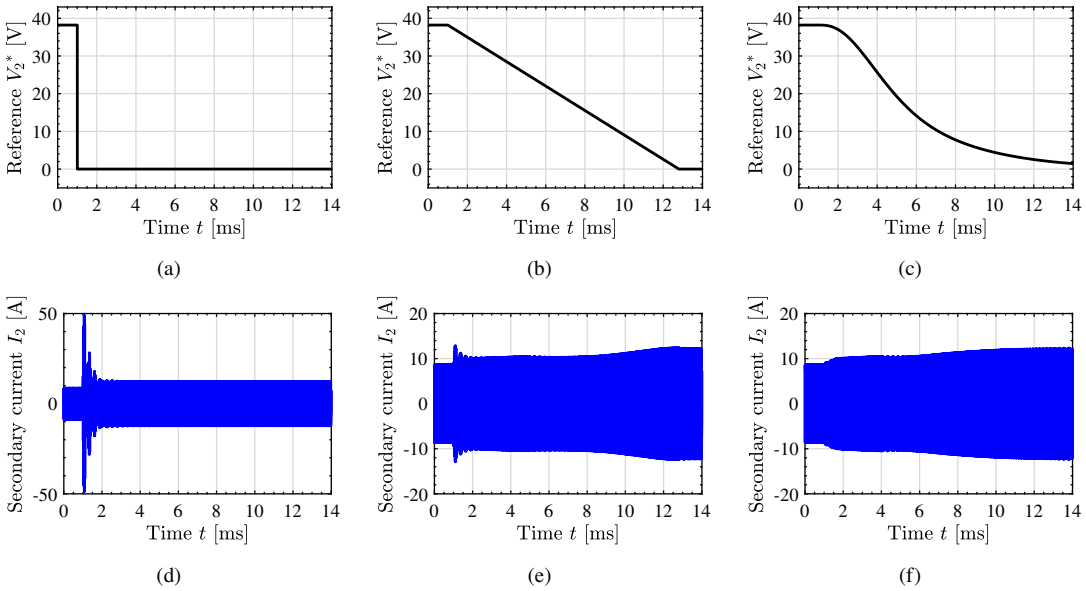

Fig. 7. Reference values of $V_2{}^*$ and simulation results of the secondary current. (a) Step-type reference (b) Ramp-type reference (c) Proposed reference (d) Result with the step-type reference (e) Result with the ramp-type reference (f) Result with the proposed reference

TABLE II
MAXIMUM VALUES OF THE SECONDARY COIL CURRENT OVERSHOOT IN THE SIMULATION

$V_2{}^*$ trajectory	Maximum current amplitude	Overshoot
Step-type	49.1 A	368 %
Ramp-type	11.4 A	8.6 %
Proposed	10.5 A	0.0 %

to suppress the overshoot ideally. TABLE II shows all the maximum values of the secondary coil current between 0 ms and 4 ms in the simulation. According to TABLE II, it can be seen that the proposed method is numerically superior to the other methods. These simulation results verify the proposed method to dump the overshoot of the secondary coil current.

With the above simulation results, experiments are performed to verify the feasibility of the proposed method. Fig. IV shows an experimental prototype setup based on the parameters listed in TABLE I. The calculation shown in Fig. 6 is implemented with a digital signal processing (DSP) controller. The reference values of $V_2{}^*$ are the same as that shown in Fig. 7. The calculated value ${d_{\rm short}}^*$ is input to the lower arm of the rectifier as the gate signal.

Figs. 9–11 show the experimental results. Figs. 9(a), 10(a), and 11(a) show the waveforms of the secondary current. Their tendencies are similar to the simulation results as shown in Fig. 7, which shows the feasibility of the proposed method.

Figs. 9(b), 10(b), and 11(b) show the waveforms of the load current. It is observed that the load current flows into the battery in Figs. 10(b) and 11(b) after the switching mode of the rectifier is changed from the RM to the SM. In terms of the transferred power control, it can be said that the step method is more accessible than the other methods; however, it is possible to control the energy including the power transferred after

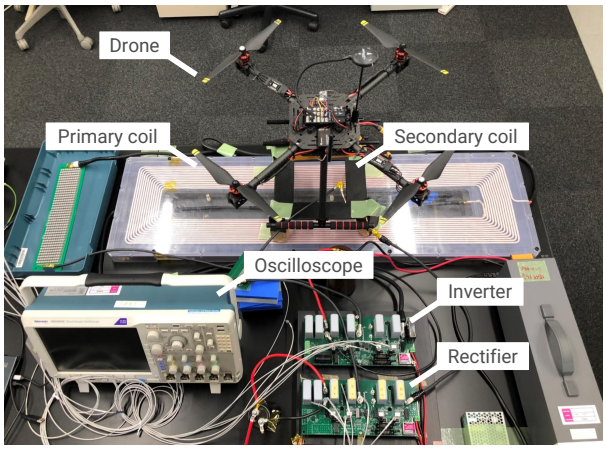

Fig. 8. Experimental prototype of the system.

changing the mode of the rectifier. In addition, there is no surge current in Fig. 11(b), which means the proposed method has no adverse effect on the battery safety. These results suggest that the proposed method is valid to suppress the coil current overshoot and control the power transferred to the battery with the SBAR system, which decreases the rated current of the rectifier so that the lighter drone system is realized.

On the other hand, it is needed to consider the case when the phase of the gate signal shifts from the state as shown in Fig. 5 because the gate signal is not synchronized with the secondary current. According to Fig. 12, the coil current overshoot can be suppressed even if the phases of the gate signal and the secondary current are shifted by $\frac{\pi}{2}$ from the state as shown in Fig. 5. This result suggests that (9) is robust to the fluctuation of the model which assumes that the phases of the gate signal and the secondary current match as shown in Fig. 5.

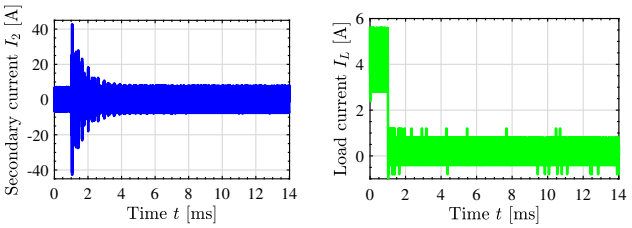

(a) (b)

Fig. 9. Experimental waveforms with the step-type reference value of $V_2{}^*$. (a) Secondary current (b) Load current

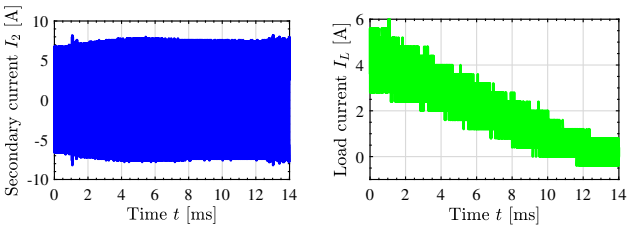

(a) (b)

Fig. 10. Experimental waveforms with the ramp-type reference value of $V_2{}^*$. (a) Secondary current (b) Load current

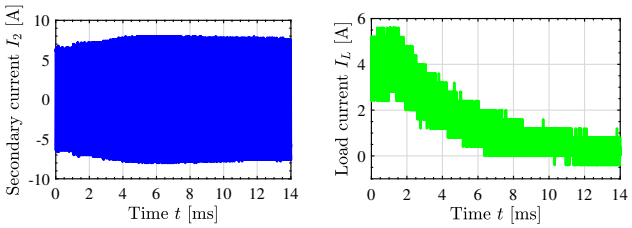

(a) (b)

Fig. 11. Experimental waveforms with the proposed reference value of $V_2{}^*$. (a) Secondary current (b) Load current

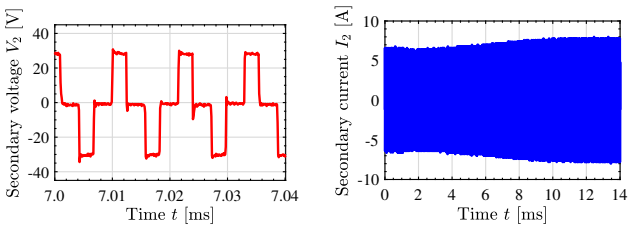

(a) (b)

Fig. 12. Experimental waveforms with the proposed reference value of $V_2{}^*$ and the phases of the gate signal and the secondary current are shifted by $\frac{\pi}{2}$ from the state as shown in Fig. 5. (a) Enlarged secondary voltage (b) Secondary current

V. Conclusion

In this paper, we proposed a novel model-based current overshoot suppression method with a two-mode operation SBAR. The control strategy is validated with the simulation and the experiment in which the maximum values of the secondary coil current overshoot are evaluated. The proposed method accomplishes a suppression of the secondary coil current overshoot, which leads to decreasing the rated current of the rectifier. By applying this method to the drone wireless in-flight charging system, the lighter secondary system is realized.

Meanwhile, it should be noted that the proposed method assumes the perfect resonance condition. The robustness to the parameter fluctuation will be improved in future studies.

VI. Acknowledgment

This work was partly supported by JST-Mirai Program Grant Number JPMJMI21E2, JSPS KAKENHI Grant Number JP18H03768, and the New Energy and Industrial Technology Development Organization (NEDO) Project Number JPNP21005, Japan.

References

[1] W. C. Brown, "Experiments Involving a Microwave Beam to Power and Position a Helicopter," *IEEE Transactions on Aerospace and Electronic Systems*, vol. AES5, no. 5, pp. 692–702, 1969.

[2] N. Takabayashi, N. Shinohara, T. Mitani, and M. Furukawa, "Rectification Improvement With Flat-Topped Beams on 2.45-GHz Rectenna Arrays," *IEEE Transactions on Microwave Theory and Techniques*, vol. 68, no. 3, pp. 1151–1163, 2020.

[3] J. M. Arteaga, S. Aldhaher, G. Kkelis, C. Kwan, D. C. Yates, and P. D. Mitcheson, "Dynamic Capabilities of Multi-MHz Inductive Power Transfer Systems Demonstrated with Batteryless Drones," *IEEE Transactions on Power Electronics*, vol. 34, no. 6, pp. 5093–5104, 2019.

[4] T. Campi, S. Cruciani, F. Maradei, and M. Feliziani, "Innovative design of drone landing gear used as a receiving coil in wireless charging application," *Energies*, vol. 12, no. 18, 2019.

[5] Z. Zhang, S. Shen, Z. Liang, S. H. Eder, and R. Kennel, "Dynamic-Balancing Robust Current Control for Wireless Drone-in-Flight Charging," *IEEE Transactions on Power Electronics*, vol. 37, no. 3, pp. 3626–3635, 2022.

[6] Y. Shao, H. Zhang, M. Liu, and C. Ma, "Explicit Design of Impedance Matching Networks for Robust MHz WPT Systems with Different Features," *IEEE Transactions on Power Electronics (Early Access)*, 2022.

[7] A. Babaki, S. Vaez-Zadeh, A. Zakerian, and G. A. Covic, "Variable-Frequency Retuned WPT System for Power Transfer and Efficiency Improvement in Dynamic EV Charging with Fixed Voltage Characteristic," *IEEE Transactions on Energy Conversion*, vol. 36, no. 3, pp. 2141–2151, 2021.

[8] G. Lovison, T. Imura, H. Fujimoto, and Y. Hori, "Secondary-side-only Phase-shifting Voltage Stabilization Control with a Single Converter for WPT Systems with Constant Power Load," *IEEJ Journal of Industry Applications*, vol. 8, no. 1, pp. 66–74, 2019.

[9] R. Okada, R. Ota, and N. Hoshi, "Novel Soft-Switching Active-Bridge Converter for Bi-directional Inductive Power Transfer System," *IEEJ Journal of Industry Applications*, vol. 11, no. 1, pp. 97–107, 2021.

[10] K. Colak, E. Asa, M. Bojarski, D. Czarkowski, and O. C. Onar, "A Novel Phase-Shift Control of Semibridgeless Active Rectifier for Wireless Power Transfer," *IEEE Transactions on Power Electronics*, vol. 30, no. 11, pp. 6288–6297, 2015.

[11] F. Zhao, C. Zhu, R. Lu, K. Song, and G. Wei, "Modeling and design of control loop with semi-bridgeless rectifier in wireless charging system," *2017 IEEE Transportation Electrification Conference and Expo, Asia-Pacific, ITEC Asia-Pacific 2017*, 2017.

[12] S. Nagai, T. Fujita, H. Fujimoto, S. Tsuge, and T. Hashimoto, "Efficiency Evaluation of Receiving Current Control Using Pulse Density Modulation for Dynamic Wireless Power Transfer," *2021 IEEE PELS Workshop on Emerging Technologies: Wireless Power Transfer, WoW 2021*, 2021.

[13] D. Gunji, T. Imura, and H. Fujimoto, "Basic study of transmitting power control method without signal communication for Wireless In-Wheel Motor via magnetic resonance coupling," *2015 IEEE International Conference on Mechatronics, ICM 2015*, pp. 317–322, 2015.